PAPER REF: 4711

CHARACTERIZATION OF X60 STEEL GRADE UNDER ULTRA LOW CYCLE FATIGUE LOADING

João Pereira[1 (*)], Abílio de Jesus[2], José Xavier[2], António A. Fernandes[1]
[1]IDMEC-LAETA, Faculdade de Engenharia da Universidade do Porto,
Rua Dr. Roberto Frias, 4200-465 Porto, Portugal.
[2] IDMEC-LAETA, Departamento de Engenharias, Escola de Ciências e Tecnologia da Universidade de Trás-os-Montes e Alto Douro, 5001-801 Vila Real, Portugal.
[3] CITAB, Universidade de Trás-os-Montes e Alto Douro, 5001-801 Vila Real, Portugal.
(*)*Email:* joao7dc@gmail.com

ABSTRACT

An investigation to study the ultra-low cycle fatigue (ULCF) behaviour of the X60 piping steel grade is reported. The ULCF damage process shows characteristics of both monotonic and low cycle fatigue (LCF) damage mechanics, therefore the understanding of these two damage mechanisms is important. An experimental program was carried out to derive ULCF data for notched specimens. Additionally, monotonic and LCF results were generated for smooth and notched specimens. Image based techniques, such as 2D-Digital image correlation (DIC), was used in monotonic tensile tests and ULCF tests, allowing the evaluation the full field displacements in the specimens surface. Finite element analyses of the non-linear plastic behaviour of steel specimens were also performed, the parameters of the different plasticity models being identified. The performance of several damage models was finally assessed.

Keywords: Ultra-low cycle fatigue, damage mechanics, DIC, finite element modelling.

INTRODUCTION

Pipelines exposed to extreme load actions (e.g. seismic cyclic action, soil settlements) may suffer significant plastic deformations leading to monotonic ductile fracture or fatigue fracture for a reduced number of cycles (N_f<100 cycles). The failure for a number of cycles lower than 100 has been named as ultra-low cycle fatigue (ULCF) or extremely low-cycle fatigue to distinguished it from low-cycle fatigue (LCF) regime, since ULCF damage mechanisms are different of those from LCF.

Concerning to monotonic damage behavior of steel components, there are already several models proposed in the literature capable of describing the material behavior. Gurson-Tvergaard-Needlman (Gurson, 1976) model based on porous plasticity, the empirical criteria proposed by Johnson and Cook (Johnson, 1985), Bay and Wierzbicki (BW) model (Wierzbicki, 2005), the Wilkins model (Wierzbicki, 2005) and the Cockcroft-Latham model (Wierzbicki, 2005) among others, have been used to model the monotonic ductile damage. Some of these models show a dependency of damage on the three invariants of the stress tensor. In the LCF damage only the second invariant of the stress/strain has deserved the main interest for multiaxial stress states.

ULCF involves damage mechanisms with characteristics from both monotonic and LCF damages, since some of the monotonic/LCF models parameters (e.g. stress triaxiality, the equivalent fracture) are involved in the ULCF models calibration. In contrast to monotonic and LFC damages, ULCF models are less developed. No guidelines are available about the most suitable fracture criterion for a particular application and how to calibrate the ULCF models for a given material.

An experimental program including monotonic, LCF and ULCF tests was carried out on smooth and notched specimens. The use of the different specimen configurations allowed distinct stress triaxialities levels and equivalent strain at fracture, which are important parameters for monotonic and ULCF models calibration, to be studied.

Digital image technique was used in both monotonic and ULCF experimental tests, to assess the displacement and strain fields in the specimen surface. This data was evaluated and then used for the calibration of the numerical plasticity models and respective validation. The plasticity models used in numerical simulations are based on associate J2 plasticity theory. A plasticity model with isotropic hardening was used for monotonic modeling while kinematic hardening was considered for cyclic loading.

In the present work, several models were assessed for fatigue life prediction, using ULCF data, generated for X60 piping steel grade. In particular, the classical Coffin-Manson relation (Coffin, 1971; Manson, 1974), the Kanvinde-Deierlein model (Kanvinde, 2007) and the Xue (Xue, 2007) model are assessed in this study.

FATIGUE MODELS

The empirical model proposed by Coffin and Manson (Coffin, 1971; Manson, 1974) is widely used for fatigue life prediction, under low-cycle fatigue regime. The plastic strain amplitude $\Delta\varepsilon^P / 2$ is related with the number of cycles to failure, N_f as follows:

$$\frac{\Delta\varepsilon^P}{2} = \varepsilon_f^{'}(2N_f)^c \tag{1}$$

$\varepsilon_f^{'}$ and c are is the fatigue ductility coefficient and c is the fatigue ductility exponent (Coffin, 1971; Manson, 1974). According to some authors (Xue, 2007), Coffin-Manson relation does not give a satisfactory prediction under ULCF regime, for several metals. They report a fatigue life over prediction when the Coffin-Manson relation is used in ULCF. This model is used in this work and their parameters are identified using specifically two series of smooth specimens, namely plane and round bar configurations of X60 steel, tested under low-cycle fatigue loading.

With respect to the proposition by Kanvinde and Deierlein (2007), it is based on micromechanical behavior of voids, which was a generalization of a model for monotonic ductile damage. Metallic materials contain voids in its microstructure, which may grow under the action of the plastic deformation. Race and Tracey (1969) reported that, for a single spherical void in an infinite continuum, the void growth rate can be described by Eq. (2):

$$dR / R = C\exp(1.5\eta)d\varepsilon_P \tag{2}$$

where R is the average void radius, C is a material constant, η define the stress triaxiality as referred above and $d\varepsilon_p = \sqrt{(2/3)\, d\varepsilon_{ij}^p d\varepsilon_{ij}^p}$ is the incremental equivalent plastic strain. The void radius *R*, can be expressed in terms of the ratio with respect to the initial void radius, R_0, and integrating Eq. (2) the following expression is obtained (Kanvinde and Deierlein, 2007):

$$\ln\left(R/R_0\right) = \int_0^{\varepsilon_p} C \exp(1.5\eta) d\varepsilon_P \tag{3}$$

Assuming void growth to be the controlling parameter of the monotonic fracture, the failure criterion for monotonic damage, is based in the critical size of the void radius and may be expressed as (Kanvinde and Deierlein, 2007):

$$\ln\left(R/R_0\right)_{monotonic}^{critical} = \int_0^{\varepsilon_p^{critical}} C \exp(1.5\eta) d\varepsilon_P \tag{4}$$

In order to derive a fracture criterion based on micromechanical behavior of voids, the void growth index $VGI_{monotonic}$, can be related with its critical value $VGI_{monotonic}^{critical}$, as follows:

$$\ln\left(R/R_0\right)_{monotonic}^{critical} / C = VGI_{monotonic} = \int_0^{\varepsilon_p} \exp\left(1.5\eta\right) d\varepsilon_p > VGI_{monotonic}^{critical} \tag{5}$$

Eq. (5) is the basis of the void growth model for monotonic loading, based on the stress triaxiality and accumulated plastic strain. $VGI_{monotonic}^{critical}$ is considered a material constant.

For cyclic loading, critical regions of the component experiences alternating - positive and negative - stress triaxialities. When triaxiality is positive, voids will grow; inversely, when triaxiality is negative, voids will shrink (average void radius will reduce) (Kanvinde and Deierlein, 2007). Thus, the sign of the stress triaxiality is used to differentiate tensile or compression loading excursion. While the sign of the triaxiality governs the voids growth or shrinkage, the magnitude of triaxiality and the equivalent plastic strain govern the rate of voids growth/shrinkage (Kanvinde and Deierlein, 2007). For a cyclic loading, Eq. (2) can be rewritten in the following more general form:

$$dR/R = sign(T) C \exp\left(\left|1.5T\right|\right) d\varepsilon_p \tag{6}$$

The void growth/shrinkage during cyclic loading is captured by the integration of Eq. (6) over tensile compressive excursions of loading (Kanvinde and Deierlein, 2007). The loading cycles can be subdivided into tensile and compressive, based on the sign of triaxiality. The evolution of void radius along the cyclic loading, for tensile and compressive excursions is expressed by the Eq. (7) (Kanvinde and Deierlein, 2007):

$$\ln\left(R/R_0\right)_{cyclic} = \sum_{tensile\, cycles} C_1 \int_{\varepsilon_1}^{\varepsilon_2} \exp\left(\left|1.5T\right|\right) d\varepsilon_p \; - \sum_{compressive\, cycles} C_2 \int_{\varepsilon_1}^{\varepsilon_2} \exp\left(\left|1.5T\right|\right) d\varepsilon_p \tag{7}$$

Following the same convention that previously allowed defining the monotonic void growth index, for cycling loading the void growth index is defined as follows:

$$VGI_{cyclic} = \sum_{tensile\, cycles} \int_{\varepsilon_1}^{\varepsilon_2} \exp\left(\left|1.5T\right|\right) d\varepsilon_p \; - \sum_{compressive\, cycles} \int_{\varepsilon_1}^{\varepsilon_2} \exp\left(\left|1.5T\right|\right) d\varepsilon_p \tag{8}$$

VGI_{cyclic} increases and decreases during cycling, however this parameter cannot assume negative values. If VGI_{cyclic} decreases to zero, it remains at zero until a subsequent "tensile" cycle increases its value above zero (Kanvinde and Deierlein, 2007). Similarly to monotonic ductile fracture, ULCF failure occurs when VGI_{cyclic} exceeds a critical value, that is $VGI_{cyclic} > VGI_{cyclic}^{critical}$. Kanvinde and Deierlein proposed, for the critical cyclic void growth index $VGI_{cyclic}^{critical}$, an exponential decay function of the critical monotonic index. To compute the $VGI_{cyclic}^{critical}$ it is important to distinguish the equivalent plastic strain that increases over the entire loading and damage variable $\varepsilon_p^{accumulated}$ that is defined as the equivalent plastic strain that is accumulated up to beginning of each tensile path of loading (Kanvinde and Deierlein, 2007). Therefore, the increment of equivalent plastic strain during the current tensile cycle does not contribute to the damage that occurs within that loading increment. The equivalent plastic strain accumulated during the entire cycle only contributes to void growth such that for each tensile cycle, VGI_{cyclic} is compared to a constant value of $VGI_{cyclic}^{critical}$. This relation is described as follows, where λ is treated as a material-dependent damage coefficient (Kanvinde and Deierlein, 2007).

$$VGI_{cyclic}^{critical} = VGI_{monotonic}^{critical} \exp\left(-\lambda \varepsilon_p^{accumulated}\right) \tag{9}$$

Regarding to the model for ULCF proposed by Xue (Xue, 2007) it is based Coffin-Manson relation and assuming linear damage summation, according to Miner's rule. The damage related to the Palmgren-Miner's is defined from the relative reduction of deformability to quantify the plastic damage accumulation (Xue, 2007):

$$D = \frac{4n\Delta\varepsilon_p}{4N\Delta\varepsilon_p} = \frac{n}{N} \tag{10}$$

where $\Delta\varepsilon_p$ is the plastic strain amplitude, n is the current number of cycles and N is the number of life cycles. Concerning to the Coffin-Manson relation can be expressed in an alternative way in Eq. (11), where C and k are materials constants:

$$\Delta\varepsilon_p \cdot N^k = C \tag{11}$$

The previous equation can be used in the limit to model the monotonic plastic failure. In that case $N = 1/2$, $C = \varepsilon_f / 2^k$ and $\Delta\varepsilon_p = \varepsilon_f$. ε_f is considered the plastic strain at fracture. The equivalent plastic distortion was introduced by Xue in order to define the cyclic plastic damage. This parameter is based on the current three principal components of the plastic strain tensor, as presented in Eq. (12). The equivalent plastic distortion should be distinguished from the equivalent plastic strain. The equivalent plastic strain accounts for the plastic strain accumulation along the loading history.

$$\varepsilon_d = \sqrt{\frac{2}{3}}\sqrt{\varepsilon_1 + \varepsilon_2 + \varepsilon_3} \tag{12}$$

By differentiation of Coffin-Manson for monotonic loading case and knowing that the incremental plastic distortion is the same that the equivalent plastic strain for each proportional loading path (Xue, 2007), a power law damage rule is obtained:

$$dD = m\left(\frac{\varepsilon_d}{\varepsilon_f}\right)^{(m-1)} \frac{1}{\varepsilon_f} d\varepsilon_p \tag{13}$$

where m is defined as $m = 1/k$. Integrating Eq. (13) along the plastic loading excursion, results the plastic damage potential function for materials obeying Coffin-Manson relation:

$$\Psi\left(\frac{\varepsilon_d}{\varepsilon_f}\right) = \left(\frac{\varepsilon_d}{\varepsilon_f}\right)^m \tag{14}$$

Based on experimental evidences, Xue proposed an alternative damage potential, valid for fatigue life prediction in ULCF regime (Xue, 2007):

$$\Psi\left(\frac{\varepsilon_d}{\varepsilon_f}\right) = \frac{e^{\lambda\frac{\varepsilon_d}{\varepsilon_f}} - 1}{e^{\lambda} - 1} \tag{15}$$

where λ is a damage parameter, which is determined by fitting the experimental results under ULCF domain $\left(N_f \le 100\,\text{cycles}\right)$. Differentiating Eq. (15), results the number of fatigue cycles as function of strain amplitude:

$$N = \frac{1}{2}\frac{e^{\lambda} - 1}{e^{\lambda\left(\frac{\Delta\varepsilon_p}{\varepsilon_f}\right)} - 1} \tag{16}$$

However, Xue verified that neither the power law nor the exponential damage rules fits the complete range of life cycles from both LCF and ULCF regimes. Therefore a new function, based on m and λ parameters, is presented to predict fatigue life cycles from $1/2 \sim 10^4$ (Xue, 2007). In order to derive a new damage potential function for the entire fatigue regime, the influence of the plastic damage accumulation and the exponential damage rule for the ULCF regime can be coupled through the joint effect of m and λ parameters, as follows:

$$\Psi\left(\frac{\varepsilon_d}{\varepsilon_f}\right) = \frac{e^{\lambda\left(\frac{\varepsilon_d}{\varepsilon_f}\right)^m} - 1}{e^{\lambda} - 1} \tag{17}$$

The damage rate is derived from Eq. (17), thus the strain *versus* life relationship is governed by the Eq. (19):

$$dD = \frac{m\lambda\left(\frac{\varepsilon_d}{\varepsilon_f}\right)^{(m-1)} e^{\left(\lambda\left(\frac{\varepsilon_d}{\varepsilon_f}\right)^m\right)}}{\left(e^{\lambda} - 1\right)} \frac{d\varepsilon_p}{\varepsilon_f} \tag{18}$$

$$N = \frac{1}{2}\frac{e^{\lambda}-1}{e^{\lambda\left(\frac{\varepsilon_d}{\varepsilon_f}\right)^m}-1} \tag{19}$$

DIGITAL IMAGE CORRELATION

Digital image correlation (DIC) measures full-field displacements of an object by comparing the similarity of speckled features in images acquired at distinct mechanical configurations. The reference image (undeformed configuration) is typically divided into correlation domains named subsets. The size of these subsets must guarantee that the spatial distribution of pixel grey levels represents a unique pattern with suitable contrast and isotropy. Moreover, the subset size should be conveniently chosen in a compromise between correlations and interpolation errors. The DIC method can be used on both 2D and 3D (stereovision) configurations (ARAMIS; Xavier, 2012). DIC-2D measures the in-plane displacements of a (quasi-)planar surface of interest, and it requires the usage of only one digital camera. DIC-3D provides both in-plane and out-of-plane displacements (although with different resolutions), and, conventionally, two identical optical systems (i.e., digital camera, lenses, aperture, focal length…) are used. The stereovision system has the advantage of taking into account (at least at a certain extent) both parasitic out-of-plane movements and contraction effect (Poisson's effect) that may occur during a tensile mechanical loading. Moreover, it can be more properly applied to specimens with moderate curved surfaces. However, it requires a calibration procedure of the stereovision system, which is time consuming.

In this work, the ARAMIS® v6.02 system by GOM was used (ARAMIS). The optical devices and measuring parameters are summarized in Table 1. In this photomechanical set-up, one digital camera was coupled with a telecentric lens. This type of lens is more expensive and eventually larger and heavier than normal lenses of similar focal length, but has the advantage of keeping invariant the magnification factor of the optical system for a given range of working distance.

The surface of the specimen was painted in order to define a speckled pattern suitable for DIC measurements. The surface was firstly polished using 300-grit sandpaper. A background white matte paint was then applied followed by a spread distribution of black painting using an airbrush. The typical speckled pattern obtained with this marking technique is shown in Figure 1, along with the histogram of the image. As it can be seen, the pixel gray-level is relatively spread over the dynamic range of the camera sensor.

Taking into account the size of the region of interest, the optical magnification and the quality of the speckle, the facet size (number of pixels per subset) and the facet step (distance between adjacent facet centres) were set to 15×15 pixels2 and 13×13 pixels2 , respectively (Table 1). The strain field was numerically evaluated from the displacement field by point-wise least-square approximation using a base length of 5 subsets (Table 1). The displacement and strain resolution associated to the DIC measurements were, respectively, of the order of 2×10-2 pixel and 0.02%. This evaluation was carried out based on rigid-body movements (Xavier, 2012)

Table 1 Optical system components and measurement parameters.

	Experimental tests
	DIC-2D
CCD Cameras	
Model	Baumer Optronic FWX20 (8 bits, 1624x1236 pixels)
Shutter time (ms)	0.7
Frequency (Hz)	0.5
Lenses	
Model	Telecentric lens TC 23 36
	Field of View: 29.3x22.1 mm
	f/8
Lighting	High intensity LED spotlight: CCS HSL-58SW-D300
Working distance (mm)	103.5
Conversion factor (mm/pixel)	0.0045
ARAMIS 2D	
Facet size (pixels)	15x15
Step size (pixels)	15x15
Strain step - gauge length (subsets)	7x7

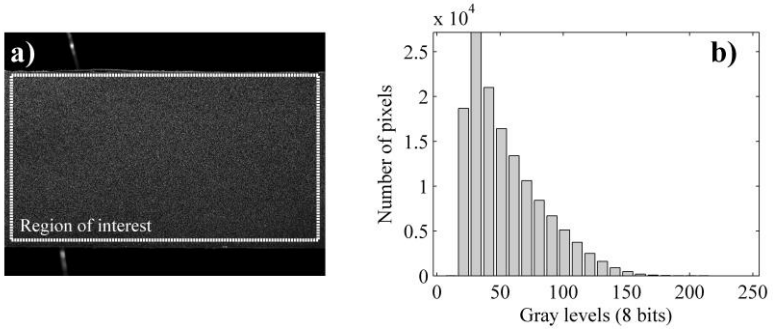

Fig.1 (a) Speckle pattern (region of interest of 27.9×15.6 mm^2; conversion factor of 17.9 μm/pixel) and (b) histogram of the image used in the digital image correlation measurements.

FINITE ELEMENT ANALYSES

In order to identify the required parameters involved in the monotonic and ULCF models, elastoplastic numerical simulations were performed in ABAQUS 6.12® (Abaqus, 2012). The plasticity models were based on J2 yield stress criterion. For monotonic tensile tests simulations, a plasticity model with multilinear isotropic hardening was considered while a non-linear kinematic (Chaboche) hardening plasticity model was used for cyclic tests analysis. Taking into account the existing symmetry planes specimens, only 1/8 of the specimen geometry was modeled using 8-noded isoparametric solid element, C3D8R (Abaqus, 2012). The total length of the finite element models corresponded to the gauge length of the dynamic extensometer used in the experimental work to measure/control the displacements.

The stress-strain curve illustrated in Figure 2 has been used to define the multilinear isotropic hardening while the parameters based on cyclic curve fitting used to define the kinematic hardening behaviour are expressed in the Table 2.

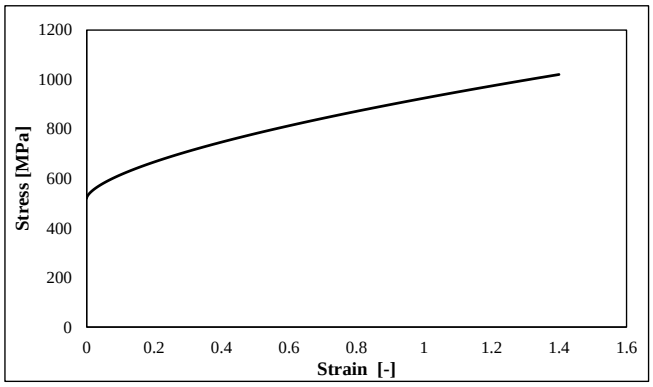

Fig. 2 Stress-strain curve in plasticity model with isotropic hardening.

Table 2. Parameters of plasticity model with kinematic hardening.

σ_{yield} [MPa]	C_1	C_2	C_3
400	52000	2000	500
	γ_1	γ_2	γ_3
	450	80	2.5

MONOTONIC TENSILE TESTS

As referred above, ULCF involves some damage features similar to the monotonic ductile mechanisms of materials. In order to identify the fracture parameters associated with each specimen configuration tested under ULCF regime, monotonic tensile tests were performed in four sets of notched plane specimens that are illustrated in Figure 3. The experimental program was carried out on a servo-hydraulic INSTRON 8801 (rated to 100kN) test machine at room temperature under a cross-head velocity of 1mm/min. The longitudinal relative displacement of the specimens was measured using an extensometer with limit displacements of ±2.5 mm with a base gauge length of 12.5 mm. This extensometer allows the measurement of an ultimate longitudinal strain of 20%.

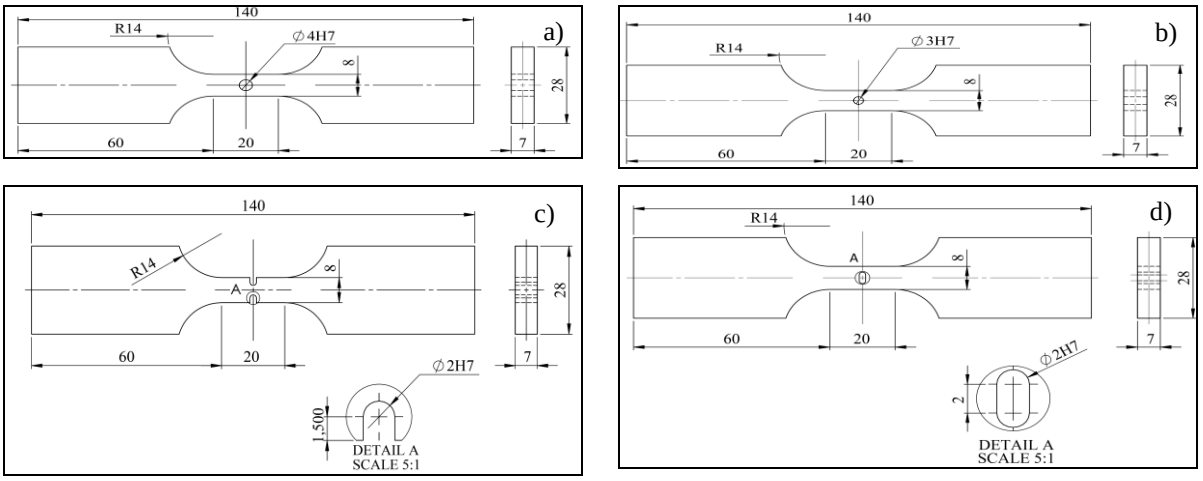

Fig. 3 Geometries of notched plane specimens of X60 steel: a) CHB series; b) CHS series; c) SN series; d) OH series (mm).

Different notched severities were considered for the referred specimens in order to obtain different stress triaxialities levels, critical monotonic void growth index as also different equivalent strains at fracture. The recorded load-displacements curves are illustrated in the Figure 4 together with the numerical curve obtained for each specimen. The elastic, plastic region and loss of strength capacity due to necking effect and damage of the specimens is clearly observed. The plasticity model with isotopic hardening introduced in the finite element model is capable of defining the loss of strength capacity at some extent, caused by a necking effect. However, the final damage degradation is not captured by the plasticity model. A satisfactory agreement between experimental and numerical behavior is verified at least for the damage onset.

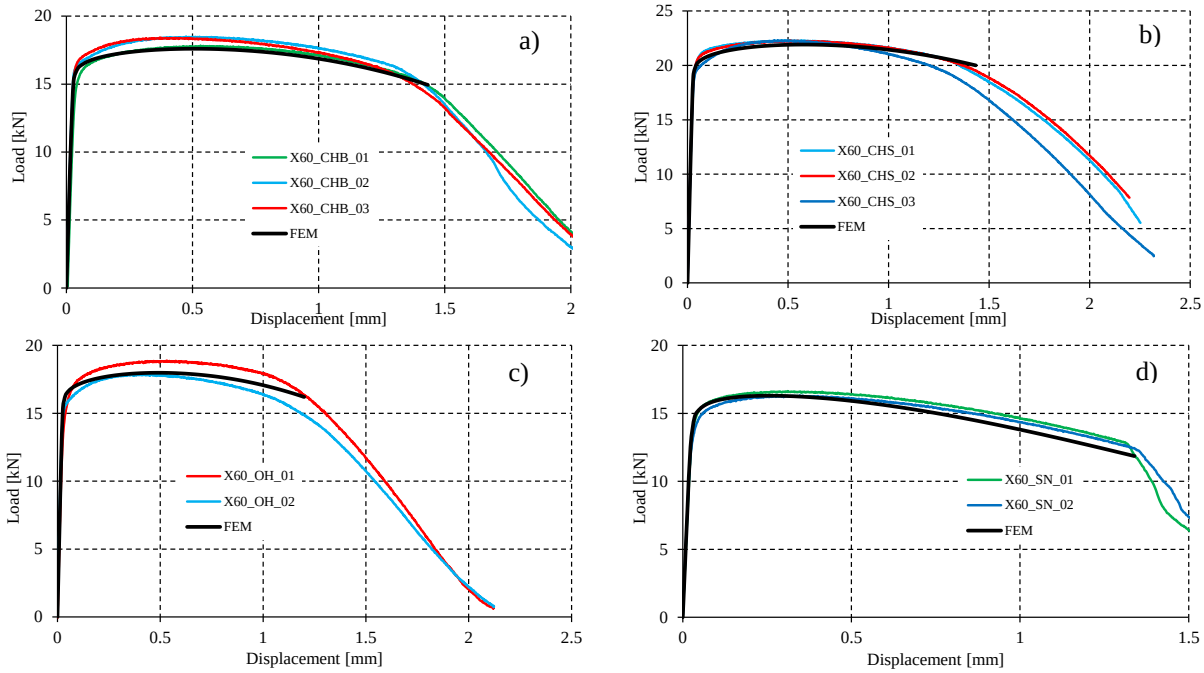

Fig. 4 Load-displacements curves of notched plane specimens of X60 steel: a) CHB series; b) CHS series; c) OH series; d) SN series.

The finite element analysis allowed the generation of the history of the parameters for the entire loading at the specimens fracture locus. Thus, the average stress triaxiality, the critical monotonic void growth index as also the equivalent strain at fracture were computed for each series. These results will be used later on in the ULCF models calibration.

Digital image correlation was used in the monotonic tensile tests. As described above, these image techniques allow the measurement of the field information for the region of interest. For the same load values, the strain field along to load direction obtained from DIC is compared with the finite element model results in the Figure 5. A good correlation is found between numerical and experimental correlation across the region of interest. This results also supported the boundary conditions related with specimen symmetry, applied in the finite element model.

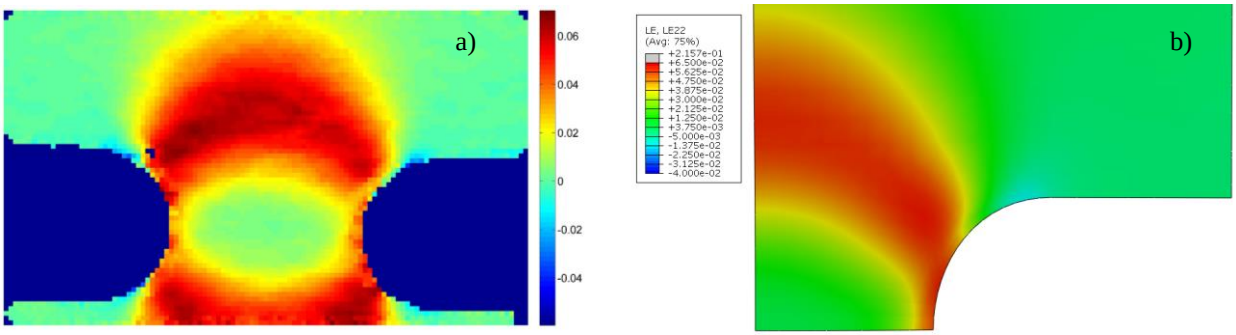

Fig. 5 Strain field along load direction (SN specimen, load= 16.61kN): a) experimental – DIC; b) numerical – FEM.

LCF TESTS

In this section, the LCF behavior of X60 steel is evaluated using cyclic tests performed on round bar (RB) and dog-bone (SP) specimens, illustrated in Figure 6. Fatigue tests were also performed on a servo hydraulic INSTRON 8801 universal test machine, under strain control with strain ratio $R_\varepsilon = -1$ and $R_\varepsilon = 0$. The strain *versus* life data of both series was analyzed together and presented using relations between the strain amplitudes and the number of reversals until crack initiation $2N_i$. The strain components, elastic and plastic, are accounted independently by the Basquin (Basquin, 1910) and Coffin-Manson relations, respectively. Following these definitions, Morrow (Morrow, 1965) relation can be expressed as follows:

$$\frac{\Delta\varepsilon}{2} = \frac{\Delta\varepsilon^E}{2} + \frac{\Delta\varepsilon^P}{2} = \frac{\sigma_f^{'}}{E}\left(2N_i\right)^b + \varepsilon_f^{'}\left(2N_i\right)^c \tag{20}$$

where $\sigma_f^{'}$ is the fatigue strength coefficient, b is the fatigue strength exponent and E is the Young modulus. The other parameters have been introduced before. In order to identify the Morrow parameters (see Table 3) for X60 steel, the global results were plotted together and represented in Figure 7. A good agreement between the experimental data and predictions is verified. The number of cycles to failure was deliberately limited between 10^2 and 10^4, which is in accordance with the LCF regime.

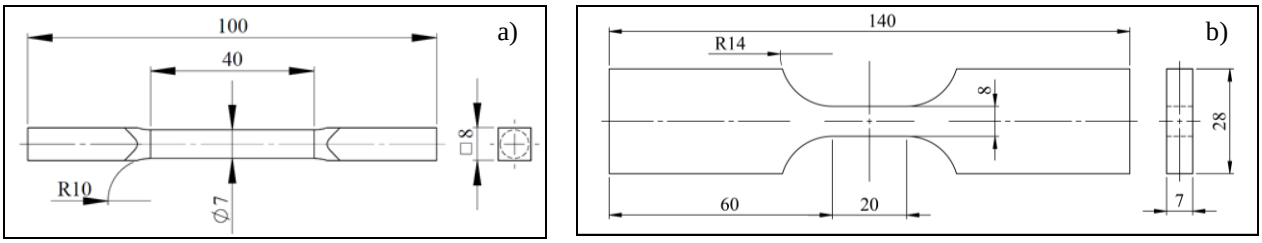

Fig. 6 Geometries of: a) round bar specimens (RB); b) smooth plane specimens (SP) (mm).

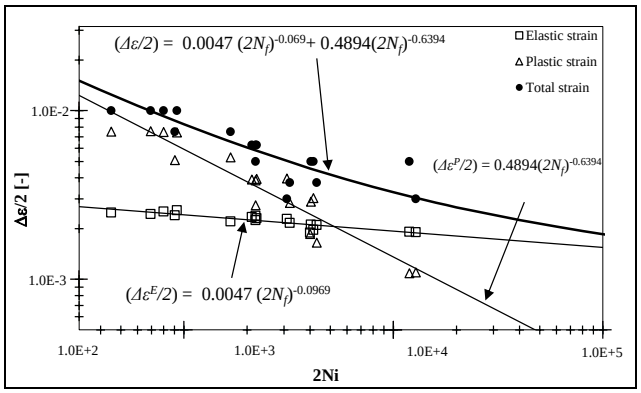

Fig. 7 Strain-life curves, for smooth round and smooth plane specimens.

Table 3. Morrow constants obtained from the LCF tests performed on smooth specimens of X60 steel.

σ'_f [MPa]	b	R^2
959.64	-0.0969	0.7945
ε'_f	c	R^2
0.4894	-0.6394	0.8928

ULCF TESTS

ULCF cyclic tests were performed on four series of notched specimens presented in Figure 3, under local (gauge) displacement control, with two displacement ratios of $R_\delta = -1$ and $R_\delta = 0$. The finite element analysis was used to obtain the stress and strain field histories at the critical regions, and thereby to compute the parameters involved in ULCF models, described above.

As previously stated, Coffin-Mason is usually used to predict the fatigue life under LCF domain. In order to investigate its performance for ULCF regime, a multiaxial strain approach was used to correlate the experimental data. The equivalent plastic strain (Kalnins, 2006) was used to compute the new CM constants ($\varepsilon'_f = 0.4086;\ c = -0.7216$) using LCF data from smooth specimens. Afterwards, this procedure was applied to the specimens tested under ULCF. The comparison between the experimental results and the predictions based on the CM model with multiaxial strain definition is illustrated in Figure 8. According Figure 8, CM relation does not give a satisfactory life prediction for ULCF regime. This data arrangement does not agree with literature which states that CM model tend to overestimate the fatigue life in the ULCF regime (Xue, 2007; Hatanaka, 1984). Based on this assumptions the CM model underestimates the fatigue lives in the ULCF regime. A reason for this apparent discrepancy is the use of different geometries (stress triaxialities) in ULCF and LCF tests.

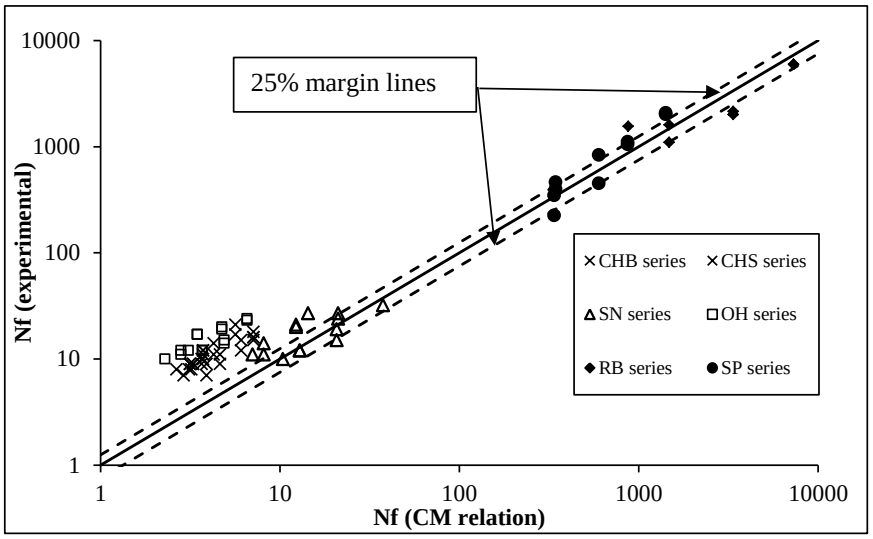

Fig. 8 Experimental number of fatigue cycles *versus* Coffin-Manson prediction with multiaxial approach.

Supported on the numerical simulations of the ULCF tests, the ratio between the critical cyclic and critical monotonic void growth index was computed for each specimen. Based on these results and the accumulated plastic strain until the failure, the cyclic damage parameter, λ, included on the damage function was obtained. Relations between the cyclic damage parameter, the strain at fracture as also the critical monotonic void growth index are identified and expressed in the Table 4. Since the damage parameter is related with specimen geometry, a new exponential function is proposed to define the critical cyclic void growth index, as follows:

$$VGI_{cyclic}^{critical} = VGI_{monotonic}^{cyclic} \times \exp\left[-C_1 \exp\left(-C_2 \varepsilon_f\right) \varepsilon_p^{accumulated}\right] \tag{21}$$

where C_1 and C_2 are the material constants and the critical monotonic void growth index becomes a damage parameter dependent on the component geometry, as presented in the Table 4. This new approach of KD model assumes a relation between the cyclic damage parameter λ and the fracture strain of each set of specimen. To compute the material constants, C_1 and C_2, the cyclic damage parameter was plotted against the fracture strain of each specimens using an exponential function to correlate these variables, as illustrated in Figure 9.

The number of fatigue cycles obtained with the new proposal of the KD model is compared with experimental data in the Figure 10. Overall, the comparisons indicate that the new approach of KD model predicts the number of cycles until crack initiation with good accuracy (fatigue life prediction within a 25% range).

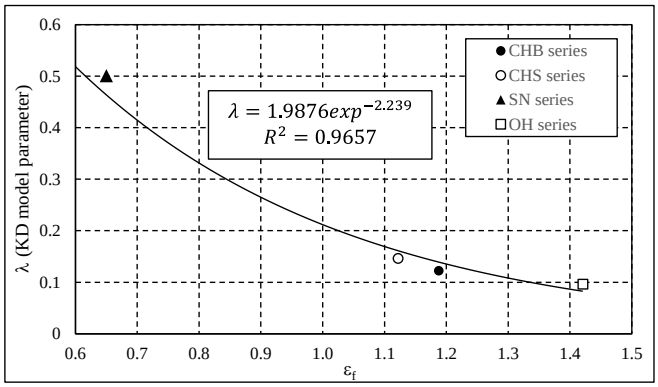

Fig. 9 Cyclic damage parameter versus fracture strain for each set of specimens.

Table 4. Monotonic fracture parameters and cyclic damage parameter.

Specimen	VGI	ε_f	λ
CHB	2.300	1.188	0.122
CHS	2.297	1.122	0.146
SN	5.957	0.650	0.501
OH	2.434	1.421	0.096

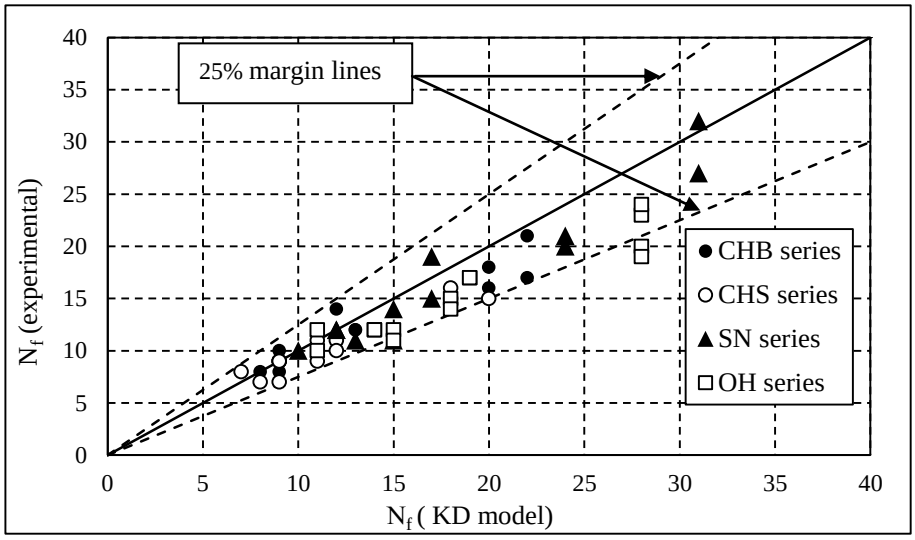

Fig. 10 Experimental number of cycles *versus* calculated number of cycles by modified KD model.

With respect to the Xue model, it was used to predict both the ULCF and LCF fatigue life. This model was originally developed for cyclic tests under a strain/displacement ratio $R_\delta = 0$. However, in according to the equivalent plastic distortion evolution for cyclic tests with strain ratio $R_\delta = -1$, Eq. (19) can be rewritten as follows:

$$N = \frac{1}{4}\frac{e^{\lambda}-1}{e^{\lambda\left(\frac{\varepsilon_d}{\varepsilon_f}\right)^m}-1} \tag{22}$$

Finite element models provides the principal plastic strain components used to compute the equivalent plastic distortion amplitude as also the fracture strain under tensile loading. Figure 11 illustrates the plastic distortion amplitude *versus* number of fatigue cycles, for the four notched specimens series tested under ULCF and smooth specimens tested under LCF. A good agreement between the experimental data and the prediction lines for $R_\delta = 0$ and $R_\delta = -1$ is verified. Both m and λ were computed by fitting the experimental $\Delta\varepsilon_d - N_i$ data. Using Eq. (19) and Eq. (22) for cyclic tests under strain ratios $R_\delta = 0$ and $R_\delta = -1$, respectively, the number of cycles until crack initiation was computed in accordance with Xue's model formulation and plotted against the experimental data, for ULCF and LCF data.

This comparison is established in the Figure 12 and it was verified that this model is able to predict fatigue life in both LCF and ULCF (detailed view in Figure 13) regimes, being the best predictions presented in this paper.

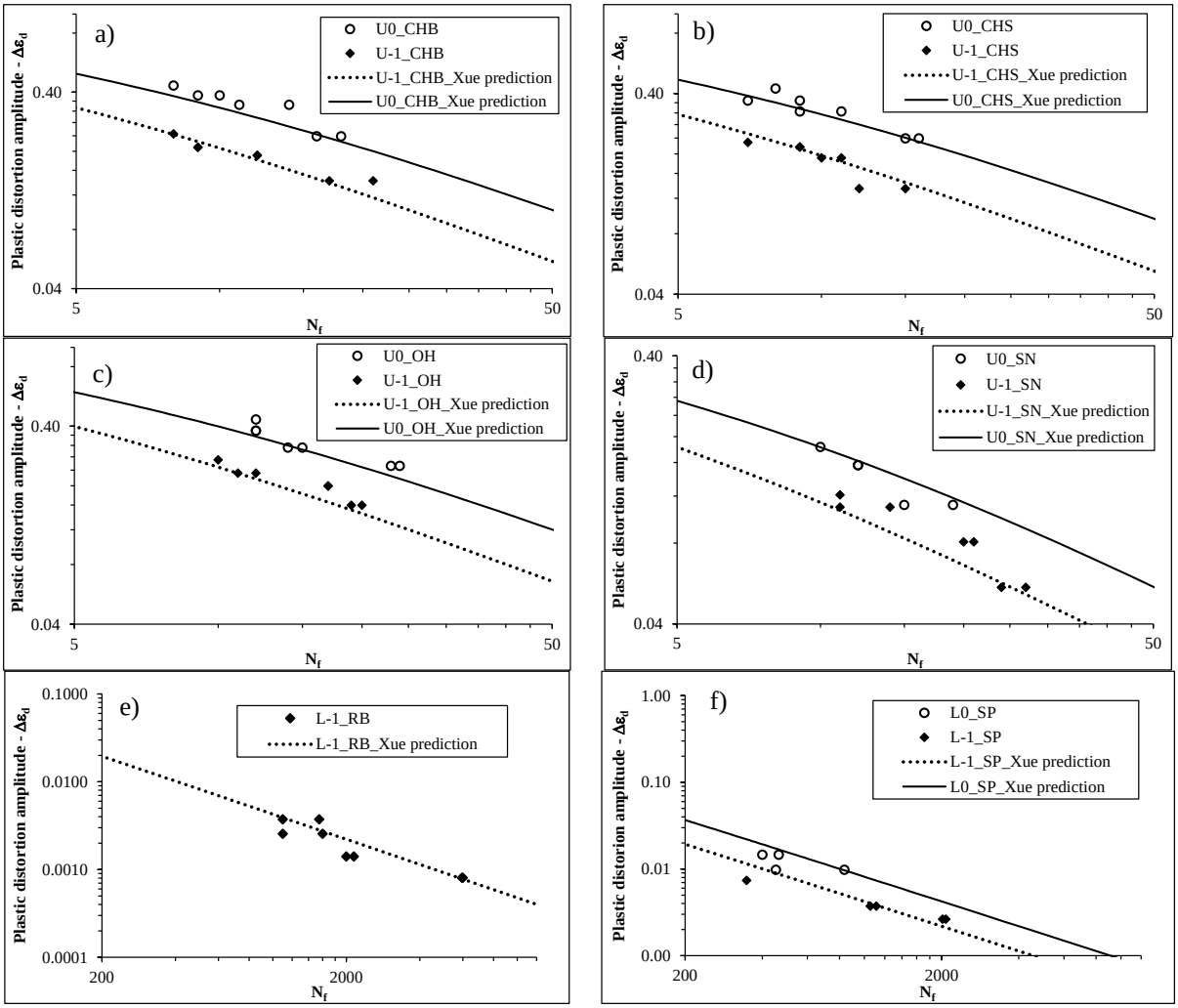

Fig. 11 Plastic distortion amplitude versus number of cycles for ULCF tests, including Xue predictions: a) CHB series; b) CHS series; c) OH series; d) SN series; e) RB series; f) SP series.

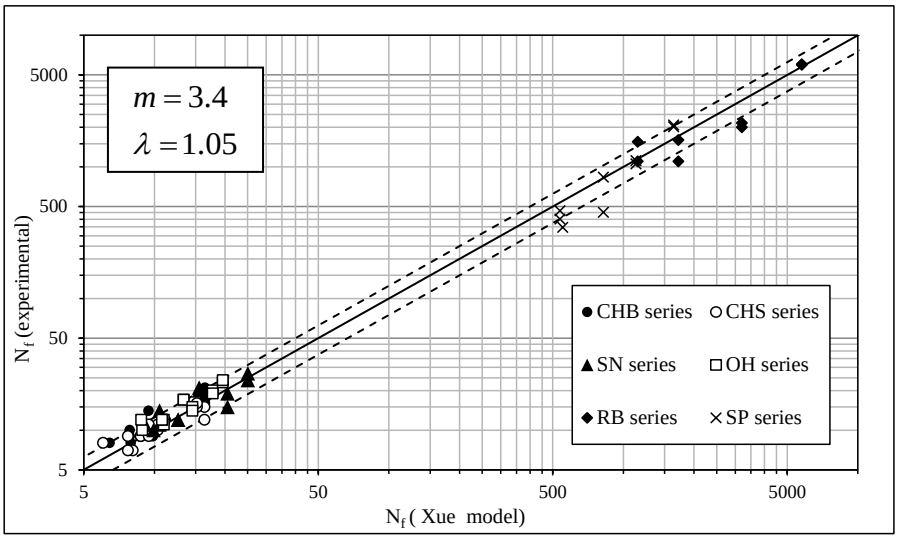

Fig. 12 Experimental number of cycles versus calculated number of cycles by Xue model.

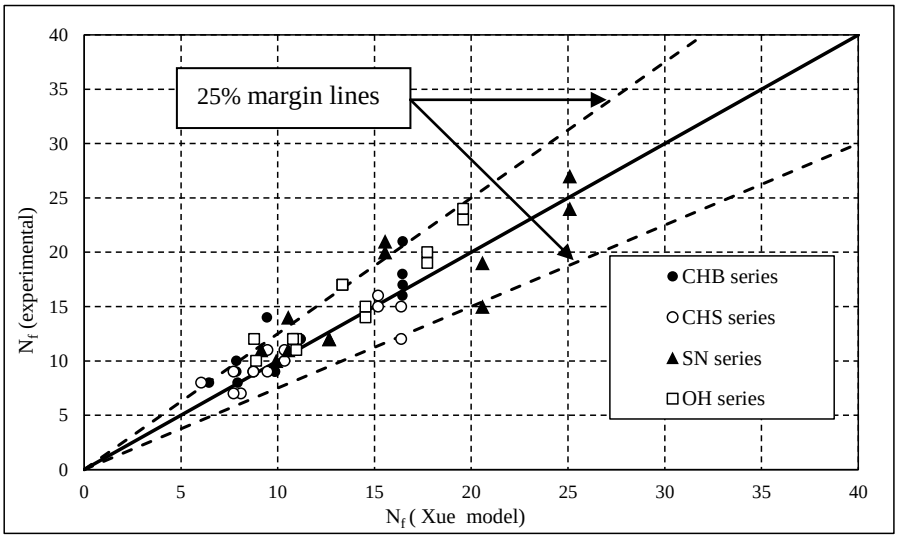

Fig. 13 Detailed view of ULCF prediction based on Xue model.

Digital image correlation was also used in the ULCF tests. In order to capture the specimen's surface at tensile and compressive "peaks" the loading cyclic path was defined as function of image acquisition frequency. Thus, the entire process loading history can be fully-monitored by digital image correlation with this experimental procedure. Following, the incremental displacements and strain field along load direction for the first compressive path are illustrated for a CHS specimens´ series in Figure 14.

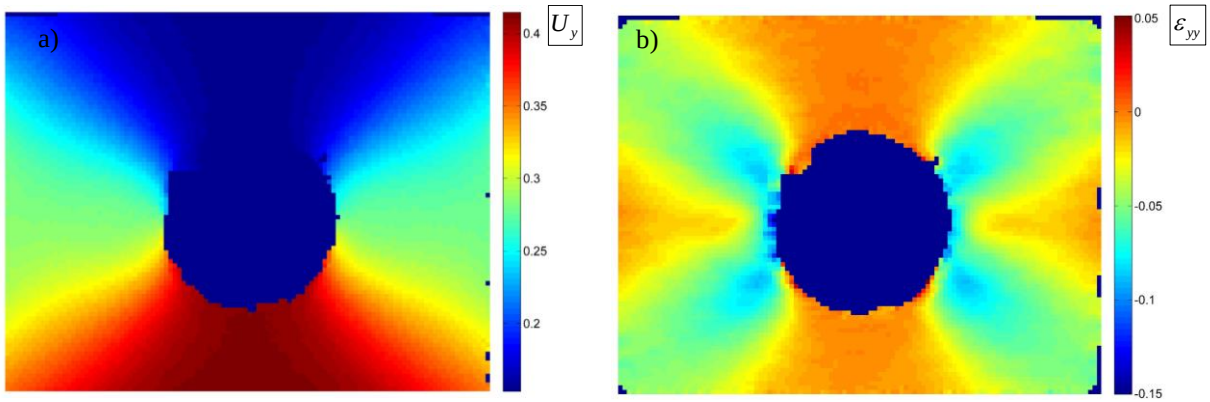

Fig. 14 Incremental full field displacements (a) and strain (b) for the first compressive excursion.

CONCLUSIONS

This paper reported the ULCF behavior of the X60 steel using an experimental program performed on notched specimens. Since monotonic properties are also required to model ULCF, additional monotonic tensile tests on same notched specimens were performed. In order to obtain the strain-life relation of X60 steel in the LCF, tests on smooth round and plane specimens were conducted.

The experimental program was supported with digital image correlation allowing the computation of the displacement/strain field at the specimen surfaces. These results require additional developments in order to validate the finite element models. Concerning the fatigue tests, DIC data can be used to model the entire cyclic loading, providing the displacement values on the boundaries of the finite element models.

With respect to the finite element analysis, isotropic and kinematic hardening plasticity models were calibrated, through inverse procedures. Finite element models provided the history of the parameters involved in the monotonic and fatigue damage models, such as equivalent plastic strain, stress triaxiality, among others.

Existing damage models were assessed using available experimental data. The Coffin-Manson model underestimates the fatigue life of the notched details under ULCF, even using a multiaxial approach. Since tested geometries in ULCF and LCF regime are not the same, this procedure cannot be used to assess the over prediction of Coffin-Mason relation in ULCF domain. Concerning the KD model, a new function is proposed for $VGI_{cyclic}^{critical}$, which provides the relation between cyclic damage parameter, λ and the fracture strain, ε_f, which in turn depends on specimens geometry and loading conditions. This new consideration allows a good precision in fatigue life prediction. The Xue model was used to estimate the fatigue life in LCF and ULCF regimes, with a good agreement between numerical and experimental results. Although this model has been developed for fatigue tests with $R = 0$ it can be also used for $R = -1$ as demonstrated in this work. The best predictions for ULCF were obtained using the Xue model.

REFERENCES

Gurson AL. Continuum theory of ductile rupture by void nucleation and growth. Part I: Yield criteria and flow rules for porous ductile media. Journal of Engineering Materials and Technology, 1977, 99(1): 2-15.

Johnson GR, Cook WH. Fracture characteristics of three metals subjected to various strains, strains rates, temperatures and pressures. Engineering Fractures Mechanics, 1985, 21(1):33-48.

Wierzbicki T, Bao Y, Lee Y-W, Bai Y. Calibration and evaluation of seven fracture models. International Journal of Mechanical Sciences, 2005, 47:719–43.

Coffin Jr LF. A note on low cycle fatigue/laws, Journal of Materials JMLSA, 1971, 6(2):388–402.

Manson SS. Behaviour of materials under conditions of thermal stress. NACA-TR-1170, National Advisory Committee for Aeronautics, 1954.

Kanvinde AM, Deierlein GG. Cyclic void growth model to assess ductile fracture initiation in structural steels due to ultra-low cycle fatigue. Journal of Engineering Mechanics.-ASCE, 2007, 133(6):701-712.

Xue L. A unified expression for low cycle fatigue and extremely low-cycle fatigue and its implication for monotonic loading. International Journal of Fatigue, 2007, 30:1691–1698.

Rice JR, Tracey DM. On the ductile enlargement of voids in triaxial stress fields", Journal of the Mechanics and Physics of Solids, 1969, 35:201–217.

ARAMIS commercial software. GOM (http://www.gom.com/)

Xavier J, de Jesus A, Morais J, Pinto J. Stereovision measurements on evaluating the modulus of elasticity of wood by compression tests parallel to the grain. Construction and Building Materials, 2012, 26(1):207-215.

ABAQUS. User's manual version 6.12, Hibbitt, Karlsson, and Sorensen, Inc., Providence, R.I, 2012.

Basquin OH. The Exponential Law of Endurance Tests. Proceedings of the American Society for Testing and Materials, 1910, 10: 625-630.

Morrow JD. Cyclic plastic strain energy and fatigue of metals. International Friction, Damping and Cyclic Plasticity, 1965, ASTM STP 378: 45-87.

Kalnins A. Fatigue analysis in pressure vessels design by local strain approach: Methods and Software Requirements. Journal of Pressure Vessel Technology, 2006, 128:2-7.

Hatanaka K, Fujimitsu T. Some considerations on cyclic stress–strain relation and low cycle fatigue life. Transactions of the Japanese Society of Mechanical Engineering - Part A, 1984 50(451):291–300.